

# Triple Junctions as Dislocation-Like Defects: The Role of Grain Boundary Crystallography Revealed by Experiment and Atomistic Simulation

Tobias Brink,\* Saba Saood, Peter Schweizer, Jörg Neugebauer, and Gerhard Dehm†  
*Max Planck Institute for Sustainable Materials, Max-Planck-Straße 1, 40237 Düsseldorf, Germany*

Grain boundary networks and their evolution are strongly influenced by triple junctions. The defect nature of these line defects significantly affects the properties of the network, but they have not been fully characterized to date. Here, we use scanning transmission electron microscopy combined with atomistic computer simulations to investigate a triple junction at the atomic scale in an Al thin film with  $\{111\}$  texture. Using sampling methods, we were able to construct the same junction structure as in the experiment within a computer model. We present a technique to calculate the Burgers vector of the triple junction. This allows us to connect the junction's dislocation character to the microscopic degrees of freedom of the joining grain boundaries. The junction line energy in the computer model can then be calculated using an embedded atom method potential. It follows the same laws as a bulk dislocation. Finally, we discovered a range of possible triple junctions for the observed grain boundaries, which vary in the magnitude of their Burgers vector. Interestingly, the experimentally observed junction is not the one with the smallest possible Burgers vector and energy. This suggests that the kinetics of transforming the junction line are likely too slow to be driven by the small energy contribution of the triple junction.

**Keywords:** grain boundary triple junction; degrees of freedom; Burgers vector; scanning transmission electron microscopy; molecular dynamics; grand-canonical sampling

## I. INTRODUCTION

Grain boundaries (GBs) are common and important defects in materials. Mechanical properties of metals, for example, are influenced by the amount and type of GBs in the sample [1–4]. GB networks evolve by the formation of GBs during synthesis and later by their movement [5–7]. However, GBs never end in regions of defect-free bulk material, but end instead either at surfaces or at so-called triple junctions, where three GBs meet in a line [8]. Quadruple or higher junctions are unstable [9] and the GB network in a material is thus defined by the triple junctions [5, 6]. Indeed, the properties of triple junctions in thin films, for example, might strongly influence the overall GB network [10]. The mobility of GBs is also affected by the drag of less mobile triple junctions [11–13], giving rise to the idea of GB junction engineering [14].

On the microscopic level, triple junctions represent objects that are structurally and thermodynamically distinct from GBs [15]. Depending on the macroscopic and microscopic degrees of freedom (DOFs) of the three joining GBs, the triple junction can exhibit a dislocation character (translational DOFs) and/or a disclination character (rotational DOFs) [15–17]. This defect character can interact with disconnections—responsible for GB mobility under stress [7]—and is thereby of fundamental importance for understanding GB network evolution from a mechanistic viewpoint [18, 19].

Additionally, the junction retains its own DOFs, for example with regards to its exact position, which also affect its core energy [15]. Indeed, the triple junctions must possess an energy excess over the defect-free bulk

material, but compared to the abutting GBs, it can be more or less energetically favorable [15]. There is some discussion in the literature about the latter point. It was found that atoms in triple junctions have comparable energies to GB atoms [20, 21]. Others, however, calculated or measured triple junction line energies and obtained both positive [22] and negative [23, 24] line energies. It is notable that often only a single number is provided for the triple junction energy, but if the triple junction has dislocation or disclination character, it is connected to a strain field whose energy diverges with infinite system size, like a dislocation [25].

There is also a similarity between triple junctions on one hand, and GB facet junctions [26–32] or GB phase junctions [33–35] on the other. All three are discontinuities in the DOFs of the GB. Different GB phases correspond to the thermodynamic states of a GB, characterized by distinct microscopic DOFs, but may in some cases share the same macroscopic DOFs [33, 35–41]. Facet junctions, in contrast, necessarily represent a change of macroscopic DOFs [26–32]. The two types of “double junctions” therefore also possess dislocation character and Burgers vectors [26–35] and we will draw some analogies to triple junctions in our analysis later.

In the present contribution, we investigate a specific triple junction in Al, which has been recorded by atomic-resolution scanning transmission electron microscopy (STEM). We thoroughly characterize its Burgers vector content using atomistic computer simulations with an empirical potential, which allows us to evaluate previous assertions about the nature of the triple junction line energy. Our findings for this concrete example case demonstrate methods of simulating and analyzing the triple junction and put its defect character in direct relation with the DOFs of the abutting GBs.

\* [t.brink@mpi-susmat.de](mailto:t.brink@mpi-susmat.de)  
† [dehm@mpi-susmat.de](mailto:dehm@mpi-susmat.de)

## II. METHODS/THEORY

### A. Experimental

Atomic resolution imaging of triple junctions requires precise crystallographic and geometric alignment, such that all three grains share a common zone axis (in our case  $[11\bar{1}]$ ) and the three tilt GBs meeting at the junction are oriented perfectly edge-on. To satisfy these conditions, Al films with a pronounced  $\{111\}$  texture were fabricated using the magnetron sputtering method, with the deposition parameters described in Ref. [42]. The crystallographic texture and GB types in the films were examined by electron-backscattered diffraction (EBSD) at 20 kV using a JEOL JSM-6490 secondary electron microscope (SEM).

The triple junctions of interest were extracted using Xe focused ion beam (FIB) milling performed on a Helios G3 Cx dual-beam SEM/FIB system (Thermo Fisher Scientific). The milling parameters are listed in Ref. [42]. The use of Xe ions avoids any Ga implantation at GBs, which is known to compromise the investigation of intrinsic triple junction structures in pure Al. Clean imaging of the junction structure required considerable experimental selectivity. In addition to the triple junction presented in the results section, two additional junctions were also lifted out. However, in both cases, one of the GBs was found to be locally deviated from the edge-on condition, particularly in the vicinity of the junction. This limitation occurred despite prior screening by EBSD.

The specimen was subsequently examined in STEM mode using a probe-corrected FEI Titan Themis 80-300 (Thermo Fisher Scientific) operated at 300 kV with probe currents of 70–80 pA. High-angle annular dark-field (HAADF) images were acquired using a Fishione detector with collection angles of 78–200 mrad. The images reported here were obtained by averaging 50 to 100 consecutive frames.

### B. Simulation

All simulations were performed with an embedded atom method (EAM) potential for Al [43] as downloaded from the NIST Interatomic Potentials Repository [44]. This potential was found to be the most accurate one to model GB phases in  $\Sigma 3 \langle 111 \rangle$  tilt boundaries [32] and we therefore also selected it for the present study.

In a first step, we indexed the experimental GBs and then ran a GB structure search to find the matching GB phases to the experimental observation. We used GRIP [45] to search the structures, which is a code that takes the macroscopic DOFs and constructs various GB supercells (here we used variations from  $1 \times 1$  to  $5 \times 5$  in the GB plane). The boundary conditions were periodic along the directions in the GB plane and we used open boundaries normal to the GB. The code then samples various displacements and insertions/deletions of GB atoms, runs a canonical MD simulation at random temperature with

95% probability, and finally minimizes the atomic positions with regards to the potential energy. We then ordered the resulting structures by their GB energy and found the experimentally-observed structures among the low-energy results.

We tested the stability of the GB structures by running molecular dynamics (MD) simulations at 300 K using Nosé–Hoover thermostats. The volume was scaled from 0 K to the thermal expansion of the bulk and then kept constant in the periodic directions. We used a time integration step of 2 fs for all simulations.

For comparison with the experiment, we used STEM image simulations with the abTEM code [46]. We simulated an electron probe with a voltage of 300 keV, a spherical aberration of 10  $\mu\text{m}$ , a semiangle of 18 mrad, a step size of 0.164  $\text{\AA}$ , and an annular detector range from 90 to 150 mrad. Gaussian defocus and noise was applied after the image simulations.

Afterwards, we assembled triple junctions using GBs with the same GB phases and different microscopic DOFs (that are crystallographically equivalent). The resulting sample is periodic along the shared tilt axis direction  $[11\bar{1}]$ , initially having a thickness of one unit cell. Then we cut a cylinder with free surfaces and a radius of 50 nm around the junction. In order to sample the triple junction structure, we cut out a hole of radius 3  $\text{\AA}$  around the junction center. We then randomly inserted from 8 up to 21 atoms in the hole of the donut shaped sample, using at least 10 statistically independent realizations each. For testing, we also repeated this with structures replicated 2 or 3 times along the tilt axis and inserted the appropriate larger amount of atoms in our sampling.

This resulted in a range of local densities. These structures were then minimized in two steps. First, the GB structures were made into rigid bodies to avoid GB phase transitions and cooled from 50 K to 0.1 K over 50 ps using a Langevin thermostat with a strong damping constant of 10 fs. In a second step, the GBs were made non-rigid and the system was minimized normally.

We finally tested for some triple junctions of interest that the resulting junction was stable at room temperature. For this, we ran MD simulations with the structure at 300 K for 1 ns. We observed no structural changes.

### C. Grain boundary excess properties

Triple junctions cannot exist without the abutting GBs. We will thus recapitulate the established formalisms to describe the thermodynamics and excess properties of GBs. In the present case, the bulk phase is fcc Al and does not undergo any phase changes. We can therefore limit the discussion to excess properties. For GBs, their excess free energy in a single-component system is defined as [41]

$$\gamma A = [U]_N - T[S]_N - \sigma_{33}[V]_N - A \sum_{i=1,2} \hat{t}_i \sigma_{3i} - \mu[N]_N. \quad (1)$$

Here,  $\gamma$  is the GB energy,  $A$  the GB area,  $U$  the internal energy of the system,  $T$  the temperature,  $S$  the entropy,  $\sigma_{ij}$  the stress tensor,  $V$  the volume,  $\mu$  the chemical potential, and  $N$  the number of atoms in the system. The excess shears  $\hat{t}_{1,2}$  represent the translational, microscopic DOFs of the GB and are discussed in more detail further down. We just note here that they cannot be uniquely defined [35]. The bracket notation indicates excess properties of the GB [41, 47] and is defined for any extensive property  $Z$  as

$$[Z]_N = Z - \frac{N}{N_{\text{bulk}}} Z_{\text{bulk}}. \quad (2)$$

The subscript “bulk” refers to a defect-free reference system. In this framework, it is thus  $[N]_N = 0$  and the final term of Eq. 1 is zero for single-component systems.

We note that defect thermodynamics can also be expressed in the isobaric grand canonical ensemble

$$\Phi = U - TS - \sigma_{ij}V_0(\delta_{ij} + \varepsilon_{ij}) - \mu N, \quad (3)$$

which is zero in equilibrium due to being fully Legendre transformed [48]. (Here, we use the infinitesimal strain approximation with  $V \approx V_0$ .) For non-equilibrium defects, such as GBs and their triple junctions, the resulting nonzero  $\Phi$  is equal to  $[\Phi]$ . In case the thermodynamic potential is not Legendre transformed with regard to all stress components (e.g.,  $\varepsilon_{11} = \varepsilon_{22} = \varepsilon_{12} = 0$  for our GB definition), this equality still works if  $\sigma_{ij} = 0$  in the defect-free regions for the non-transformed stresses. In this case, only the defects contribute to the strain energy. This excess strain energy of the defect then goes into  $U$ . Our definitions therefore allow us to write

$$\gamma A = [\Phi] = \Phi. \quad (4)$$

Note carefully that this is not true for other, nonzero thermodynamic potentials, such as the Gibbs or Helmholtz free energy.

We assume that the thermodynamic (meta)stability of a triple junction is dominated by its potential energy and simplify in the rest of this paper by assuming  $T = 0$  and  $\sigma_{ij} = 0$ , which can be easily calculated with molecular statics simulations. Thus, with  $U = E$ , where  $E$  is the potential energy of the system, we get

$$\Phi \approx E - \mu N \quad \text{and} \quad \Phi \approx [E], \quad (5)$$

showing that  $\mu N \approx NE_{\text{bulk}}/N_{\text{bulk}}$ .

As stated in the introduction, defects can occur in different defect phases, which can be treated with the thermodynamic framework sketched above. For GBs, these GB phases are defined by their microscopic DOFs. First, while  $[N]_N = 0$  by definition, the GB phases can differ by the occupancy of their crystallographic planes compared to the defect-free crystal. While this does not affect the thermodynamics, it leads to different GB structures and can affect the transformation kinetics [49]. We establish a planar fraction  $\hat{n}$  for a GB of area  $A$  in an orthorhombic

region with  $N$  atoms that has two sides parallel to the GB. We define [49]

$$\hat{n} = \frac{n_{\text{GB}}}{n_{\text{plane}}} \quad \text{with} \quad n_{\text{GB}} = N \bmod n_{\text{plane}}. \quad (6)$$

Here,  $n_{\text{plane}}$  is the number of atoms in a defect-free crystallographic plane with area  $A$  that is parallel to the GB. Thus,  $n_{\text{GB}}$  represents the additional or missing atoms in the GB plane relative to the bulk, and  $\hat{n}$  expresses this as a fraction that is independent of  $A$ .

Additionally, the abutting crystallites can be translated against each other. Following Winter and Frolov [35], we can define the microscopic DOFs as

$$\hat{\mathbf{t}}^{(i)} = \mathbf{d}_{\text{SC}}^{(i)} + \hat{\mathbf{B}} + \underbrace{\begin{pmatrix} 0 \\ 0 \\ [V] + n_{\text{GB}} \frac{\Omega}{A} \end{pmatrix}}_{\hat{\mathbf{C}}}. \quad (7)$$

Here,  $\hat{\mathbf{B}}$  represents the crystallographic translation between the two abutting crystallites and  $\Omega$  is the equilibrium atomic volume. In the direction normal to the GB, additional contributions stem from the excess volume  $[V]$  and from the difference in planar occupancy in the GB. These contributions can be summed for simplicity into  $\hat{\mathbf{C}}$ . There is, however, not a unique translation vector  $\hat{\mathbf{t}}$  for each GB phase: Any shift of one of the crystallites by a displacement shift complete (DSC) vector  $\mathbf{d}_{\text{SC}}^{(i)}$  (which may be zero) leads to an equivalent GB structure, albeit shifted in position. Consequently, there are a range of equivalent, but not equal, values of  $\hat{\mathbf{t}}$ . There is not an infinite number, because any translation by a vector of the coincidence site lattice (CSL) leads to an indistinguishable system, so  $\mathbf{d}_{\text{SC}}^{(i)}$  is restricted by the CSL periodicity. Furthermore, note that  $n_{\text{plane}}\Omega/A$  corresponds to a DSC vector, wherefore we require  $0 \leq n_{\text{GB}} < n_{\text{plane}}$  and thus  $0 \leq \hat{n} < 1$  for a unique definition of  $\hat{\mathbf{C}}$ .

### III. RESULTS

#### A. Observed triple junction and grain boundary phases

The experimentally observed GB triple junction is shown in Fig. 1. The three adjacent grains are oriented along a common  $[11\bar{1}]$  zone axis. We indexed the  $\langle 112 \rangle$  crystal directions as indicated. Then, we generated a list of possible CSL tilt GBs with  $[11\bar{1}]$  tilt axis and  $\Sigma < 100$  using the software from Ref. [50]. The closest matches were the  $\Sigma 3$ ,  $\Sigma 39$ , and  $\Sigma 13$  boundaries as shown in Fig. 1. All GBs are symmetric. As-indexed, the misorientations of these three GBs add up to  $0^\circ$ , meaning that there is no disclination [8, 15, 51–53] at the triple junction. This is also evidenced by the GBs following the coincidence index combination rule [8]:  $3 \cdot 13 = 39$ .

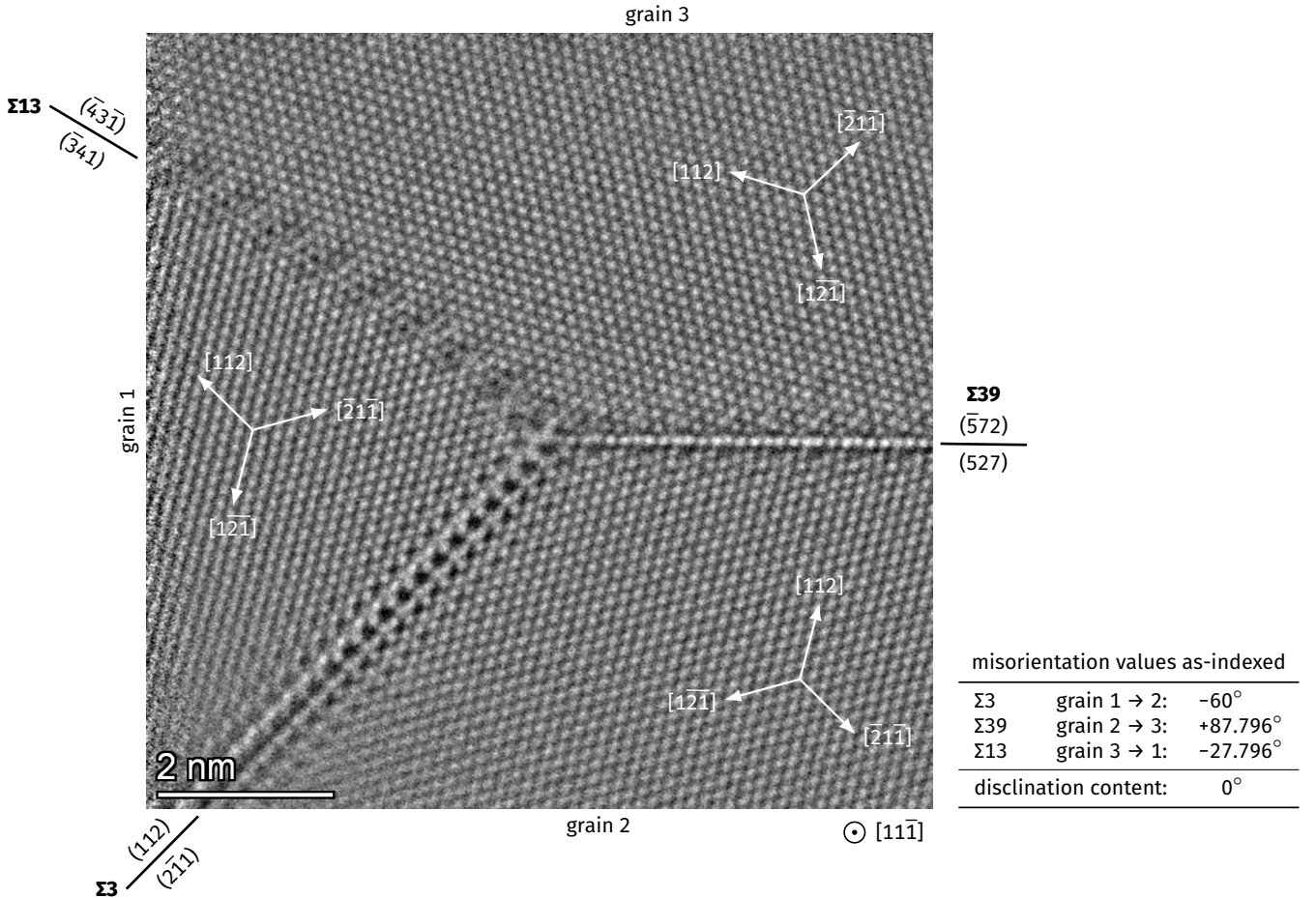


FIG. 1. HAADF-STEM image of a GB triple junction in Al. The crystallographic  $\langle 112 \rangle$  directions of the three grains were indexed and used to determine the GB planes. We found that the GBs are three symmetric  $[11\bar{1}]$  tilt GBs— $\Sigma 13$ ,  $\Sigma 39$ , and  $\Sigma 3$ —with the indicated planes. The table shows the misorientation values as indexed. Note that the cubic crystal has a threefold symmetry around  $[11\bar{1}]$  and angles  $\pm 120^\circ$  are crystallographically equivalent. We find that the misorientations add up to  $0^\circ$ , meaning that this triple junction has no disclination content.

In order to investigate the defect character of the junction in more detail, we proceeded to build an atomistic computer model. First, we ran a structure search with GRIP [45] to find the three GB structures. Detailed results of the search are listed in Supplemental Figs. S1–S3. All low-energy structures have a planar fraction  $\hat{n} = 0$ , which seems to be common for  $[11\bar{1}]$  tilt GBs [54].

The  $\Sigma 3$   $[11\bar{1}]$   $(112)/(2\bar{1}\bar{1})$  GB obtained from structure search did not perfectly match the observed GB (Supplemental Fig. S4). Some of us reported earlier that this  $\Sigma 3$  GB can have different microstates based on the local stress state [42]. This is related to the offset between  $(11\bar{1})$  planes (Fig. 2(a), right). We applied a shear stress  $\tau_{31}$  and obtained the match between STEM image and image simulation shown in Fig. 2(b,c). Such a distortion near the junction makes sense, since the  $\Sigma 3$  GB is the only GB with a large offset between  $(11\bar{1})$  planes, and the two other GBs thus exert a  $\tau_{31}$  shear stress onto the  $\Sigma 3$  GB.

The  $\Sigma 39$   $[11\bar{1}]$   $(\bar{5}72)/(527)$  GB is clearly visible in

the STEM image and matches the simulated structure (Fig. 3). We only note that the structure search revealed another structure with  $3 \text{ mJ/m}^2$  difference in the GB energy at 0 K (Supplemental Fig. S2). This structure, however, was not observed experimentally. We conclude that it either represents a microstate or that it is an artifact of the EAM potential. We use the structure from Fig. 3 for the present paper.

The  $\Sigma 13$   $[11\bar{1}]$   $(\bar{4}3\bar{1})/(\bar{3}41)$  GB exhibits some moiré patterns in the STEM image along the GB, which likely indicate that there is a GB step in the depth of the sample. We nevertheless compared the minimum-energy structure obtained in the structure search with the experimental results in Fig. 4. The motif that we marked in yellow in Fig. 4(b) is the same as in the STEM image simulation of the model structure, even though there is some noise in the center of the motif in the experiment. We further note from the simulation results that this motif is repeated three times in the periodic unit cell of the GB, being shifted each time by one atomic layer along

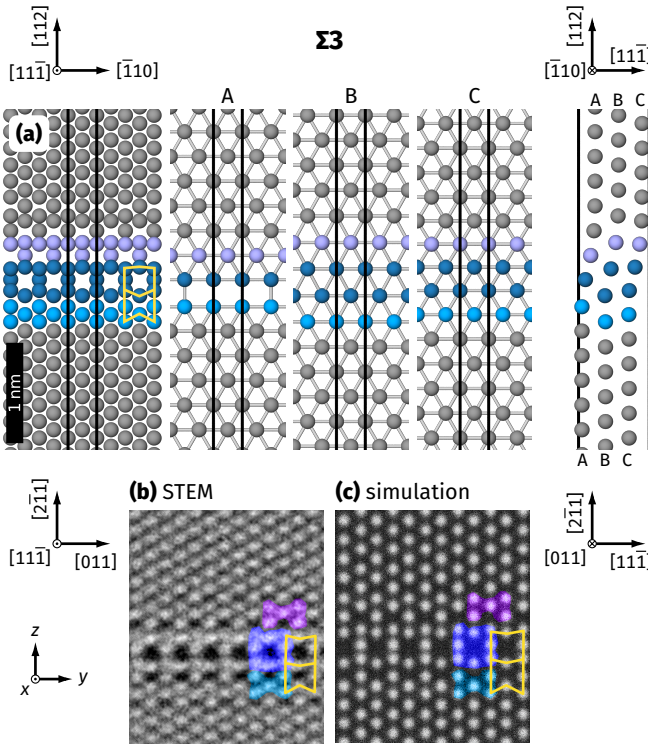


FIG. 2. Atomic structure of the  $\Sigma 3$   $[11\bar{1}]$   $\{112\}$  tilt GB. (a) Simulated structure. On the left, we show the same viewing direction as in the STEM image. The three images in the center show slices of the three nonequivalent  $(11\bar{1})$  planes A, B, and C as marked in the sideview on the right. The gray lines in the slices represent the next-neighbor bonds inside the plane, highlighting that the fcc structure in this  $\Sigma 3$  GB is only disturbed on the A plane. Color coding of the atoms highlights the (arbitrary) atomic motifs, with the dark blue atoms representing the center of the GB. An excerpt of the STEM image (b) is compared with a STEM image simulation (c). Here, we applied a stress  $\tau_{31}$  to the latter to achieve a better match. This stress is likely to also occur in the real sample, see text and Supplemental Fig. S4.

the  $[11\bar{1}]$  axis.

These GB motifs were observed and characterized earlier [55] and are typical for  $[11\bar{1}]$  tilt GBs in Al. There, motifs with no offset between  $(11\bar{1})$  planes were classified as “bow & arrow” structures, the others as “zipper”. All these GB phases have in common that  $\hat{n} = n_{\text{GB}} = 0$  and thus  $\hat{C}_{1,2} = \hat{B}_{1,2}$ ;  $\hat{C}_3 = \hat{B}_3 + [V]$  (see Eq. 7).

## B. Computer model of the junction and its energy

To construct a triple junction, we only need to rotate the obtained GB structures and join them. While there is no disclination, and therefore no gap due to angular mismatch, it stands to reason that the crystallites still cannot be joined perfectly. This is because the crystallites at a GB can be translated with regard to each other (microscopic DOFs).

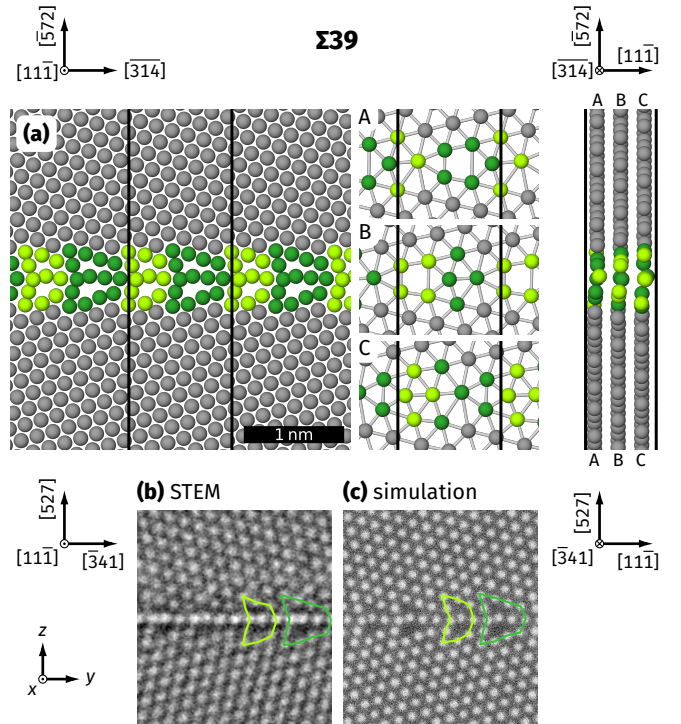


FIG. 3. Atomic structure of the  $\Sigma 39$   $[11\bar{1}]$   $\{257\}$  tilt GB. (a) Simulated structure. On the left, we show the same viewing direction as in the STEM image. The three images in the center show slices of the three nonequivalent  $(11\bar{1})$  planes A, B, and C as marked in the sideview on the right. The gray lines in the slices represent the next-neighbor bonds inside the plane. Color coding of the atoms highlights the (arbitrary) atomic motifs. An excerpt of the STEM image (b) is compared with a STEM image simulation (c).

In a first step, we thus tried to reproduce the motifs of the experimental junction. We marked certain motifs around the junction area in the STEM image (Fig. 5(a), pink atomic columns). The simulated GB structures were then shifted, combined, and overlapping atoms deleted to reproduce the arrangement of atomic motifs next to the junction core. Afterwards, a cylindrical hole was cut around the junction. For sampling, this hole was then randomly filled with various amounts of atoms and minimized. Our best match to the experimental structure is shown in Fig. 5. We performed STEM image simulations on two snapshots with  $L_x = 21.1$  nm (30 unit cells along the tilt axis) that were equilibrated at 300 K to capture the effect of phonons and thermal expansion. The STEM image simulation matches almost perfectly to the experimental image, except for the increased intensity in the center of the junction (arrows). The latter is likely due to a step of the  $\Sigma 13$  GB along the depth of the experimental sample (as discussed before in Sec. III A).

In order to rationally select a “best” structure from our sampling, we need to define a junction energy. We stay in the zero Kelvin approximation for simplicity and assume unstrained bulk crystallites. As for GBs, we can use the

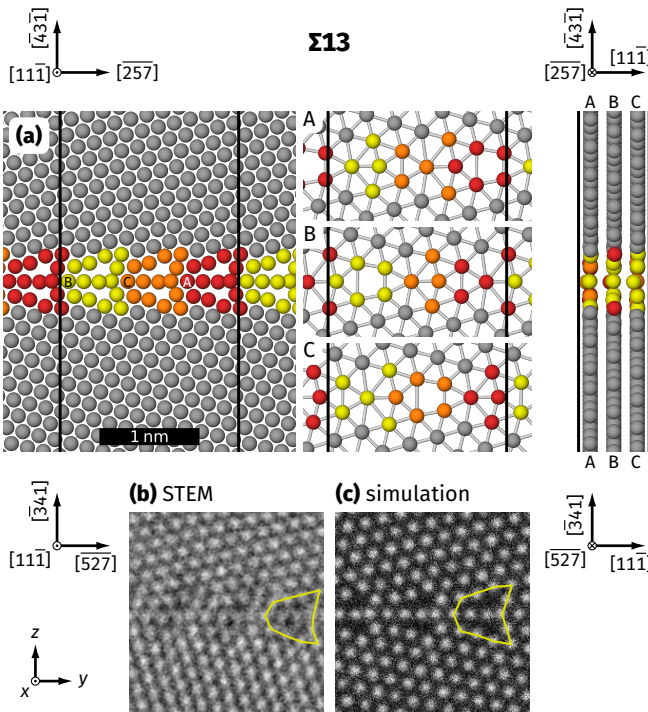


FIG. 4. Atomic structure of the  $\Sigma 13$   $[11\bar{1}]$   $\{134\}$  tilt GB. (a) Simulated structure. On the left, we show the same viewing direction as in the STEM image. The three images in the center show slices of the three nonequivalent  $(11\bar{1})$  planes A, B, and C as marked in the sideview on the right. The gray lines in the slices represent the next-neighbor bonds inside the plane. Color coding of the atoms highlights the (arbitrary) atomic motifs. An excerpt of the STEM image (b) is compared with a STEM image simulation (c).

excess energy  $[E] = E - \mu N$  (see Eqs. 2–5). Here,  $E$  is the total potential energy of the sample,  $N$  is the total number of atoms in the sample, and  $\mu$  the chemical potential, which is equal to the bulk's cohesive energy per atom at zero temperature and stress. This excess energy is calculated in a cylindrical region around the triple junction. On the atomic scale, however, the triple junction is not a line, but has a certain thickness. To be able to compare different triple junction core structures, we chose a uniform definition of the center line around which we draw the cylinder. We use the intersections of the GB planes as demonstrated in Supplemental Fig. S5(a).

Figure 6(a) shows the excess energy calculated within a cylindrical region of radius  $r$  around the assumed junction line. We can see that  $[E](r)$  has an approximately linear slope, which is close to the combined GB excess energy  $(\gamma_{\Sigma 3} + \gamma_{\Sigma 39} + \gamma_{\Sigma 13})L_x$ .

To extract the line energy, we define the GB area to extend from the triple junction to the radius  $r$  for each GB. For a thickness  $L_x$  of the sample along the tilt axis, we can thus define a line energy

$$\lambda = \frac{[E] - (\gamma_{\Sigma 3} + \gamma_{\Sigma 39} + \gamma_{\Sigma 13})A}{L_x}. \quad (8)$$

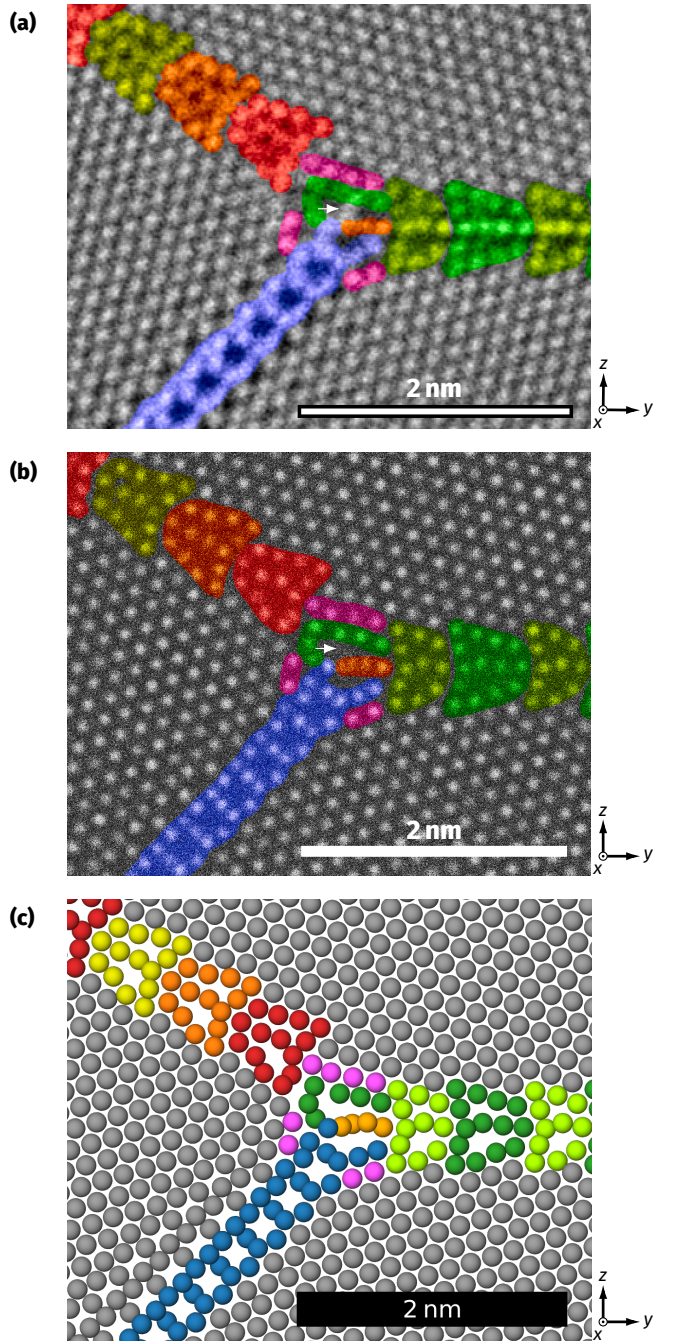


FIG. 5. Comparison of the experimental junction with the computer model. (a) Excerpt of the experimental STEM image, with false colors to highlight motifs. (b) STEM image simulation of the computer model at 300 K with the same false color highlights. (c) Snapshot of the model structure at 0 K.

(Note that we always exclude the region close to the surface to avoid an influence of the surface energy.) This is shown in Fig. 6(b). We see that the triple junction energy is not constant, but depends on the radius, indicating that the triple junction is connected to a long-range strain field that we will discuss further down.

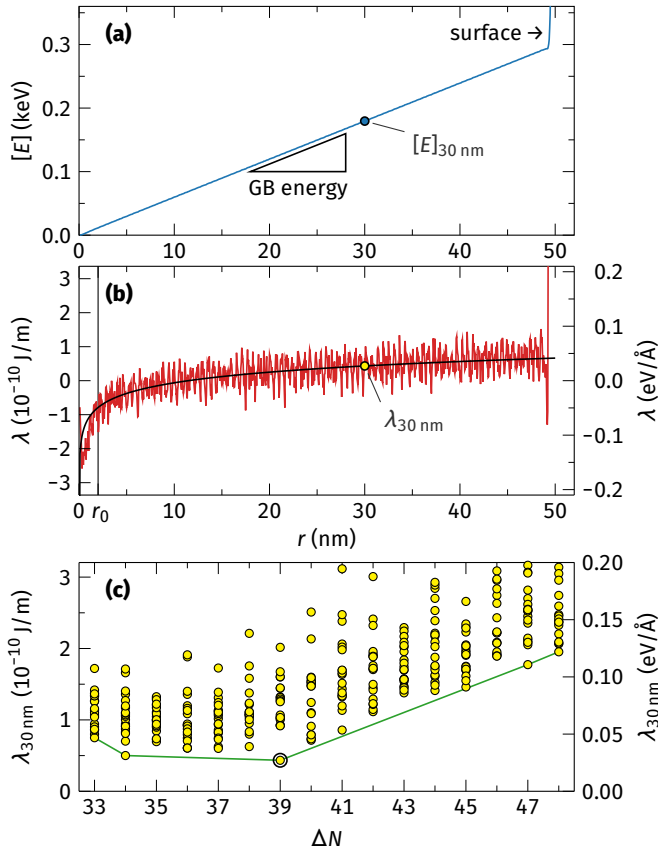


FIG. 6. (a) Cumulative excess energy  $[E]$  inside the given radius  $r$ . The slope is approximately equal to the sum of GB energies (see text). For comparison between different structures, we use the excess energy at  $r = 30$  nm (data point). (b) The line energy  $\lambda$  follows a logarithmic trend. (c) Structure sampling with different numbers of atoms  $\Delta N$  inserted into the triple junction region. These simulations were performed for a sample with a thickness of 3 unit cells along the  $x$  direction. Panels (a) and (b) show the data for the marked structure with the lowest line energy at  $\Delta N = 39$ .

For comparability, we used the line energy  $\lambda_{30\text{ nm}}$  at radius 30 nm to compare the energies of different structures during sampling (Fig. 6(c)). We chose this radius since it is sufficiently far away from the surface ( $r = 50$  nm) and the junction center. The lowest-energy structure corresponds to the best fit with experiment from Fig. 5. We verified that a different choice of junction line center shifts all line energies by the same amount (Supplemental Fig. S5), indicating that this introduces a systematic error and virtually no scatter, meaning that the choice of minimum-energy structure is robust with regards to choice of the center. Furthermore, there is a direct, linear correlation between  $[E]_{30\text{ nm}}$  and  $\lambda_{30\text{ nm}}$  so that the minimum-energy structure with either criterion is the same (Supplemental Fig. S6). Additionally, we repeated the structure search with one, two, and three unit cells along the periodic  $x$  direction, yielding the same results (Supplemental Fig. S7).

### C. Dislocation character of the triple junction

The logarithmic radial dependence of the line energy (Fig. 6(b)) implies a dislocation-like nature of the triple junction. We therefore define a Burgers circuit to extract the defect content of the junction line over the pure GBs. The dislocation content of the individual GBs depends on the macroscopic misorientation (see, e.g., Read and Shockley [56]), but does not lead to long-range strain fields [57]. To separate the junction Burgers vector content from the GBs, we will therefore make a circuit with reference to defect-free GBs. This was proposed for GB phase junctions before [33], but can be trivially extended to triple junctions.

For this, we first construct a closed loop over the triple junction in Fig. 7(a). The red lines  $t_2$  and  $t_3$  move only through fcc regions and can be calculated the same way as for a classical Burgers circuit. The GB crossings are measured in otherwise defect-free bicrystals (Fig. 7(b)–(d)). All line segments  $t_i$  are then rotated into the simulation's coordinate system as depicted in Fig. 7(a) using the relevant rotation matrices  $R_i$ . We obtain

$$\begin{aligned} \mathbf{b}_{\text{obs}} = & -R_{\Sigma 3} \mathbf{t}_{\Sigma 3} \\ & + R_2 \left( 6 \frac{a}{6} [\bar{2}\bar{1}\bar{1}] + 12 \frac{a}{6} [\bar{1}\bar{1}\bar{2}] \right) \\ & + R_{\Sigma 39} \mathbf{t}_{\Sigma 39} \\ & + R_3 \left( 5 \frac{a}{6} [\bar{1}\bar{2}\bar{1}] + 22 \frac{a}{6} [112] - \frac{a}{3} [11\bar{1}] \right) \\ & - R_{\Sigma 13} \mathbf{t}_{\Sigma 13} = (-1.002, -0.042, -0.720) \text{ \AA}. \end{aligned} \quad (9)$$

We checked that this Burgers vector is independent of the structure and amount of atoms inserted into the junction region. We will explore the relation of the junction's defect content to the GB DOFs later. Note that the GB crossings require very exact length measurements to obtain the correct Burgers vector, which is unfortunately not possible in the experiment given the measurement uncertainties and possible sample distortions.

Due to the junction line's dislocation character, the energy depends on the cylinder radius as follows [25]:

$$\lambda = K b^2 \ln \left( \frac{r}{r_0} \right) + \lambda_0. \quad (10)$$

Here,  $K$  is a prefactor including the elastic moduli of the bulk,  $r_0 = 2$  nm is the (arbitrary) core radius, and  $\lambda_0$  is the core energy. We chose the core radius to include all disturbed structural GB motifs near the junction. We obtain  $K = 3.0$  GPa and  $\lambda_0 = -0.79 \times 10^{-10}$  J/m.

The meaning of negative line energies (or core energies in the present case) has been debated. As already pointed out by King [15], the triple junction can easily be energetically favorable compared to the GBs, as long as it is still of higher energy than the defect-free bulk region. A negative line energy in no way means that the system is unstable against the formation of more triple junctions, since the formation of a triple junction necessarily requires the formation of the abutting GBs. In

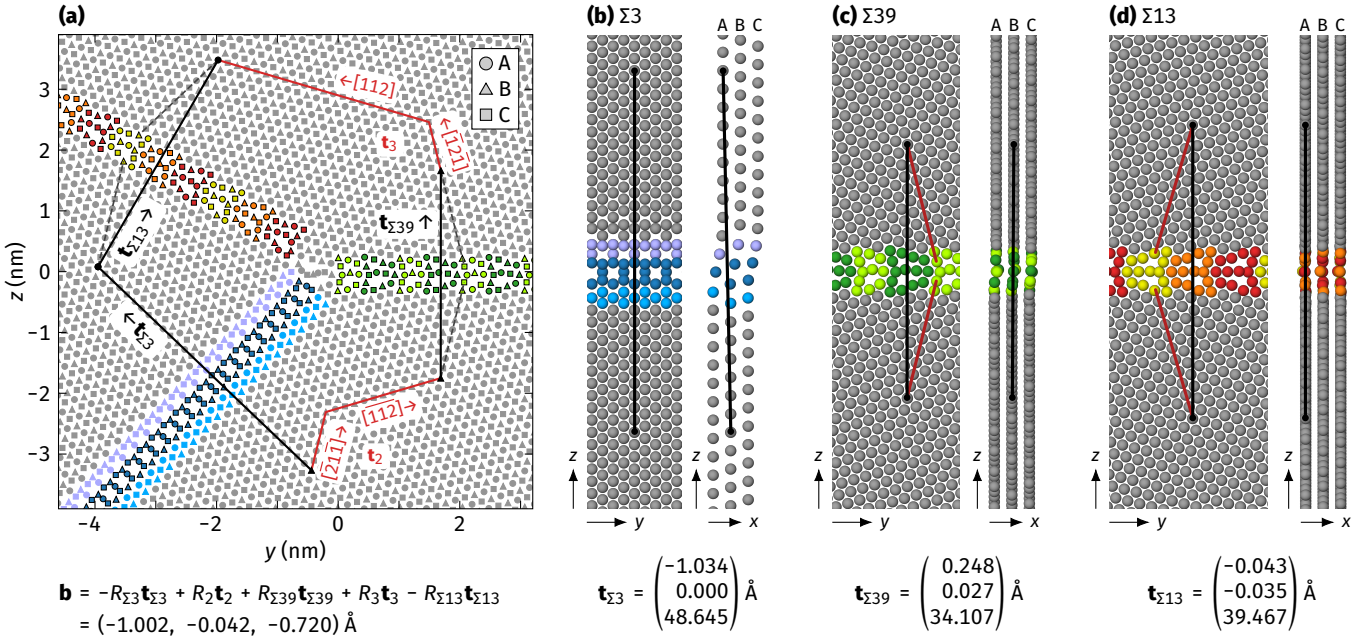


FIG. 7. (a) Burgers circuit around the triple junction that fits best to the experiment (Fig. 5). The circuit goes counter-clockwise around the  $x$  direction ( $[11\bar{1}]$  tilt axis). The red segments  $\mathbf{t}_2$  and  $\mathbf{t}_3$  of the circuit move through defect-free fcc regions. The black segments  $\mathbf{t}_{\Sigma 3}$ ,  $\mathbf{t}_{\Sigma 39}$ , and  $\mathbf{t}_{\Sigma 13}$  must be measured from defect-free reference GB structures in (b)–(d).

other words, the separation of  $[E]$  into GB energies  $\gamma$  and a line energy  $\lambda$  is arbitrary, but useful to understand the dislocation-like behavior of the junction. While the absolute defect energy of the junction line is therefore ill-defined, energy differences between junctions are nevertheless meaningful, as we saw before in Supplemental Figs. S5 and S6. Importantly, due to the logarithmic dependence in Eq. 10, the line energy diverges to positive infinity with increasing system size. The line energies are consequently always positive for sufficiently large system sizes (or grain sizes in a polycrystal).

Finally, the interatomic potential has a shear modulus  $17.6 \text{ GPa} \leq G \leq 44.1 \text{ GPa}$  (range of elastic anisotropy) and a Poisson ratio  $\nu = 0.33$ . Assuming a screw dislocation with  $K = G/(4\pi)$  [25] we estimate  $G = 37.3 \text{ GPa}$  from Eq. 10, while we obtain  $G = 24.8 \text{ GPa}$  for an edge dislocation ( $K = G/(4\pi(1-\nu))$  [25]). This lies in the expected range and further confirms the dislocation character of the GB triple junction.

#### D. Sampling the microscopic degrees of freedom

We already noted that the Burgers vector is independent of the triple junction structure. It must therefore be a result of the GBs' DOFs. While each GB structure (GB phase) is connected to specific DOFs  $\hat{\mathbf{C}}$  (see Sec. II C), there are many crystallographically equivalent realizations  $\hat{\mathbf{t}}$  of the same GB structure. The reason is that shifting one crystallite by a DSC vector will result in the same atomic arrangement within the GB,

albeit potentially on a different parallel plane in the crystal. This is limited by the CSL. Shifting one crystallite by exactly a CSL vector will leave behind a completely undistinguishable atomic structure (assuming an infinite medium, otherwise there would of course be a surface step). Thus, each GB has a large, but finite amount of DOFs that affect how the three crystallites fit together at the triple junction. If a gap remains, a Burgers vector will result because the crystallites have to deform with a long-range elastic field to close the misfit. Assuming that we express our microscopic DOFs  $\hat{\mathbf{t}}$  as the displacement of the upper crystallite compared to the lower crystallite, and assuming a counter-clockwise Burgers circuit around the junction as depicted in Fig. 1, we can express the resulting Burgers vector as

$$\mathbf{b} = -R_{\Sigma 3}\hat{\mathbf{t}}_{\Sigma 3} + R_{\Sigma 39}\hat{\mathbf{t}}_{\Sigma 39} - R_{\Sigma 13}\hat{\mathbf{t}}_{\Sigma 13}. \quad (11)$$

Here,  $R_i$  are the rotation matrices to align the GBs as found in the experimental triple junction. This is similar to the derivation of the Burgers vector at a GB phase junction [33], where two different GB structures/chemistries meet, albeit with three joining GBs.

For the given GBs, the CSL and DSC unit cells are shown in Fig. 8(a)–(c) and their basis vectors listed in Supplemental Table S-I. We can thus explore different combinations of the microscopic DOFs  $\hat{\mathbf{t}} = \hat{\mathbf{C}} + \mathbf{d}_{\text{sc}}$ , listed in Supplemental Tables S-I and S-II, to obtain different Burgers vectors. The model of the experimentally-

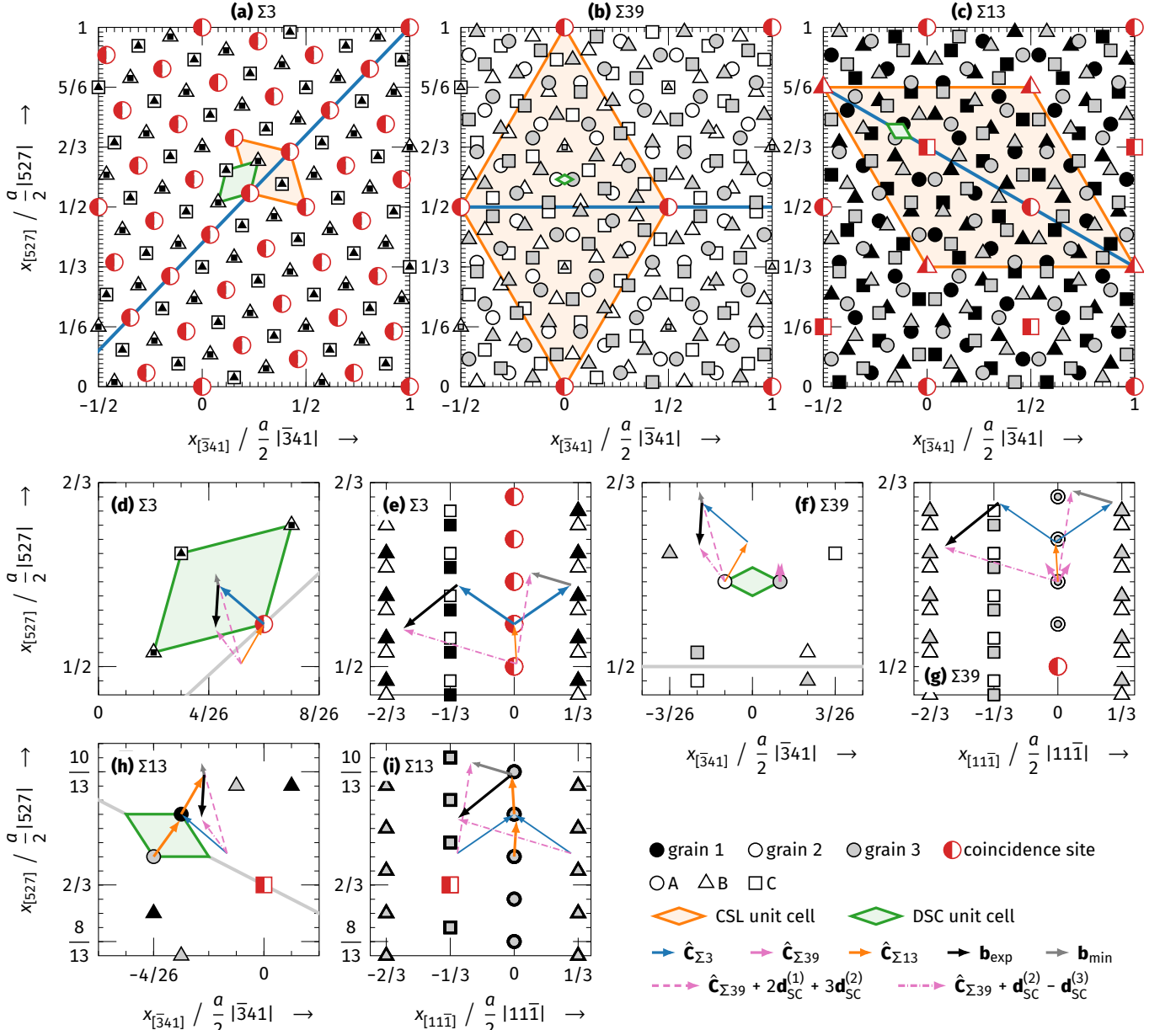


FIG. 8. Dichromatic patterns for the GBs. The indicated crystal directions belong to grain 2, i.e., the bottom crystal of the  $\Sigma 39$  GB. (a)–(c) Full dichromatic patterns, with CSL and DSC unit cells indicated. (d), (f), (h) Zooms on the DSC unit cells. (e), (g), (i) Sideviews from the  $-[\bar{3}41]$  direction. In panels (d)–(i), the smallest possible Burgers vector and the experimentally observed Burgers vector are drawn onto the dichromatic patterns in gray and black. They are shown to be sums of the microscopic DOFs  $\hat{\mathbf{t}}$  of the three GBs (colored arrows). In our chosen representation,  $\Sigma 3$  and  $\Sigma 13$  have  $\hat{\mathbf{t}} = \hat{\mathbf{C}}$ , while the  $\Sigma 39$  GB's DOFs contain additional DSC vectors (dashed arrows).

observed junction has a Burgers vector of

$$\begin{aligned}
 \mathbf{b}_{\text{exp}} &= -R_{\Sigma 3}\hat{\mathbf{C}}_{\Sigma 3-} \\
 &+ R_{\Sigma 39}\left(\hat{\mathbf{C}}_{\Sigma 39+} + \mathbf{d}_{\text{SC}}^{\Sigma 39,(2)} - \mathbf{d}_{\text{SC}}^{\Sigma 39,(3)}\right) \\
 &- R_{\Sigma 13}\hat{\mathbf{C}}_{\Sigma 13-} \\
 &= -R_{\Sigma 3}\hat{\mathbf{C}}_{\Sigma 3-} + R_{\Sigma 39}\hat{\mathbf{C}}_{\Sigma 39+} \\
 &- R_{\Sigma 13}\left(\hat{\mathbf{C}}_{\Sigma 13-} + \mathbf{d}_{\text{SC}}^{\Sigma 13,(3)}\right) \\
 &= (-1.002, -0.040, -0.717) \text{ \AA} \approx \mathbf{b}_{\text{obs}}.
 \end{aligned} \tag{12}$$

The experimentally observed triple junction thus has mixed edge/screw character, with comparable components along the triple junction line ( $x$ ) and normal to it ( $z$ ). We can see that there are different possible combinations of  $\hat{\mathbf{t}}$  for the three GBs that sum to the same Burgers vector. Here, we show two. As expected, the result matches the measured Burgers vector  $\mathbf{b}_{\text{obs}}$  (Eq. 9). Small differences are due to uncertainties when measuring the GB crossings for the Burgers circuit (Fig. 7(b)–(d)).

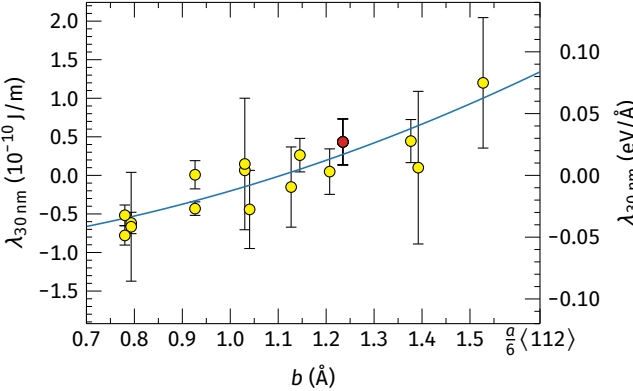


FIG. 9. Smallest line energies at  $r = 30$  nm as found by structure search for a range of Burgers vectors. The red data point belongs to the experimentally observed triple junction discussed in Sec. III B. The error bars indicate the range of the systematic error due to different choices of the triple junction center line (see Supplemental Fig. S5). The blue line is a fit of a parabola to the data.

The minimal possible Burgers vector is

$$\begin{aligned} \mathbf{b}_{\min} &= -R_{\Sigma 3}\hat{\mathbf{C}}_{\Sigma 3+} \\ &+ R_{\Sigma 39}\left(\hat{\mathbf{C}}_{\Sigma 39+} + 2\mathbf{d}_{\text{SC}}^{\Sigma 39,(1)} + 3\mathbf{d}_{\text{SC}}^{\Sigma 39,(2)}\right) \\ &- R_{\Sigma 13}\hat{\mathbf{C}}_{\Sigma 13-} \\ &= (-0.743, -0.040, 0.196) \text{ Å}. \end{aligned} \quad (13)$$

It has its largest component along the tilt axis, which is also the junction line direction, and has thus a large screw component. Both  $\mathbf{b}_{\text{exp}}$  and  $\mathbf{b}_{\min}$  are illustrated in Fig. 8(d)–(i).

There should also be a maximum Burgers vector due to the CSL periodicity, i.e.,  $\hat{\mathbf{t}}$  gets wrapped back into the CSL unit cell. When iterating over the non-equivalent  $\hat{\mathbf{t}}$  and computing the resulting Burgers vectors, we still obtain some Burgers vectors that are so large that they exceed the periodicity of the fcc lattice. Consequently, the largest possible triple junction Burgers vector is on the order of the fcc bond length, which is equal to the length of the primitive unit cell vectors of fcc. Thus  $|\mathbf{b}| \leq 2.85 \text{ Å}$  in Al, which corresponds to a full  $a/2\langle 011 \rangle$  bulk dislocation.

We move on to build several computer models of junctions with different Burgers vectors. The predicted and measured Burgers vectors matched in all cases. The resulting line energies are plotted in Fig. 9 as a function of the magnitude of the Burgers vector. While there is scatter due to the differences in core energies, the trend is roughly  $\lambda \propto b^2$ , as expected for dislocations. As already discussed in Sec. III C, negative line energies can occur, based on the system size for which the line energy is calculated. This simply means that the localized region around the junction has a lower excess energy than the joining GBs.

Using Eq. 10, we can again verify if the prefactor  $K$  fits

to the data with  $K = G/(4\pi)$  for screw dislocations [25] and  $K = G/(4\pi(1 - \nu))$  for edge dislocations [25]. The interatomic potential has a shear modulus  $17.6 \text{ GPa} \leq G \leq 44.1 \text{ GPa}$  (range of elastic anisotropy) and a Poisson ratio  $\nu = 0.33$ . Assuming a screw dislocation, the fit in Fig. 9 corresponds to a shear modulus of  $42 \text{ GPa}$ , while assuming an edge dislocation corresponds to  $G = 28 \text{ GPa}$ . This lies in the expected range and further confirms the dislocation character of the GB triple junction.

These results demonstrate that the triple junction has a dislocation character that is determined by the microscopic DOFs of the three joining GBs. The triple junction line energy follows the same trends as the energy of a bulk dislocation.

### E. Comparison to triple junction energies in literature

How do our line energies  $\lambda$  compare to previous results in the literature? Measurements of surface grooves at the triple junction [22] yielded values on the order of  $6 \times 10^{-9} \text{ J/m}$  for Cu. This number is an order of magnitude higher than the range that we found (Figs. 6 and 9). However, it is unclear to what region around the groove the measurement is sensitive, and part of what we assigned to the GB energy may be contained in this number. Computer simulations in fcc metals [23, 24] found values on the order of  $-10^{-10} \text{ J/m}$ , more in line with our results. However, depending on the Burgers vector and the radius  $r$  within which we measured the line energy including the elastic strain energy, we obtain either negative or positive values.

The literature values cannot be directly compared to ours, because these authors assumed a constant line energy without long-range elastic fields in their calculations. This is clearly visible, e.g., in Fig. 3 of Ref. [23], where the elastic strain energy was assigned to the GBs by assuming that the GB energy converges with  $r$ . In the finite-size simulation cell, it indeed looks as if the GB energy defined this way converges, but due to the logarithmic function of the strain energy, it actually diverges in infinitely-sized systems.

## IV. CONCLUSION

We observed a GB triple junction in a {111}-textured Al thin film with atomic resolution. We analyzed the defect character of the triple junction in more detail using a surrogate atomistic computer model. Our findings are:

- Triple junctions have dislocation character, i.e., a Burgers vector. They are therefore connected with long-range strain fields. We presented a method to measure the Burgers vector directly using GB reference structures. Additionally, we demonstrated for our example of a disclination-free triple junction

that this Burgers vector is a result of the microscopic DOFs of the joining GBs. There are a large number of possible combinations for the same three GBs, but the number is not infinite. This is because the periodicity of the CSL limits the distinguishable combinations.

- The magnitude of the Burgers vector is comparable to that of disconnections and not much smaller than for bulk dislocations ( $b_{\min}$  is half as big as a Shockley partial). On the one hand, this indicates that the triple junction can act as a sink or source for other line defects, and on the other hand, elastic interactions between bulk dislocations, disconnections, and triple junctions will play an important role in GB network evolution and plasticity.
- A direct consequence of the triple junction's strain field is the divergence of its line energy for infinitely-sized systems. Using an EAM potential on the computer models, we showed that the line energy follows the same logarithmic law as bulk dislocations. Any line energy that was reported as a single value in the literature is thus only meaningful when the corresponding system size is known. For different realizations of our triple junction, as well as for different system sizes, we observed both positive and negative line energies. Within a radius  $r \leq 50 \text{ nm}$  around the junction, the line energies were on the order of  $\pm 10^{-10} \text{ J/m}$ .
- Interestingly, the experimentally observed triple junction does not have the lowest possible Burgers vector and thus not the lowest possible line energy. It stands to reason that a transformation of the triple junction requires coordinated movement of the GBs and potentially diffusion to rear-

range the triple junction core region. The kinetics of this process are likely too slow to be driven by the small energy contribution of the triple junction within the experimental time frame. Additionally, any triple junction is part of a GB network. Shifting the microscopic DOFs of one GB will thus affect *two* triple junctions, coupling their excess energies. In combination with elastic junction interactions, this interdependence means that any energy minimization affects the whole GB network. Consequently, we expect that the junction types in complex GB networks are the result of junction interactions and sample history, and are thus not accurately predictable.

## V. DATA AVAILABILITY

Data to be published before final publication.

## VI. ACKNOWLEDGMENTS

Part of this work was supported by the Deutsche Forschungsgemeinschaft (DFG) within the SFB 1394, "Structural and Chemical Atomic Complexity: From Defect Phase Diagrams to Material Properties" (project ID 409476157).

*Author contributions:* TB conducted the computer simulations, analyzed the data, and wrote the initial manuscript draft. SS performed the STEM experiments. PS assisted in the analysis of the STEM results and implemented the STEM image simulations. TB, JN, and GD conceptualized the research. JN and GD secured funding within the SFB 1394, supervised the project, and contributed to discussions at all stages. All authors contributed to the preparation of the final manuscript.

---

[1] E. O. Hall, The deformation and ageing of mild steel: III Discussion of results, *Proc. Phys. Soc. London, Sect. B* **64**, 747 (1951).

[2] N. J. Petch, The cleavage strength of polycrystals, *Journal of the Iron and Steel Institute* **174**, 25 (1953).

[3] V. Randle, Grain boundary engineering: An overview after 25 years, *Mater. Sci. Technol.* **26**, 253 (2010).

[4] A. R. Krause, P. R. Cantwell, C. J. Marvel, C. Compson, J. M. Rickman, and M. P. Harmer, Review of grain boundary complexion engineering: Know your boundaries, *J. Am. Ceram. Soc.* **102**, 778 (2019).

[5] C. A. Schuh, M. Kumar, and W. E. King, Analysis of grain boundary networks and their evolution during grain boundary engineering, *Acta Mater.* **51**, 687 (2003).

[6] C. A. Schuh, R. W. Minich, and M. Kumar, Connectivity and percolation in simulated grain-boundary networks, *Philos. Mag.* **83**, 711 (2003).

[7] J. Han, S. L. Thomas, and D. J. Srolovitz, Grain-boundary kinetics: A unified approach, *Prog. Mater Sci.* **98**, 386 (2018).

[8] L. Priester, *Grain boundaries: From theory to engineering* (Springer, Berlin, Germany, 2013) Chap. 10. The Triple Junction, pp. 305–336.

[9] M. A. Fortes, Stability and dissociation of quadruple junctions in polycrystals, *Interface Sci.* **1**, 147 (1993).

[10] M. J. Patrick, G. S. Rohrer, O. Chirayutthanasak, S. Ratanaphan, E. R. Homer, G. L. Hart, Y. Epshteyn, and K. Barmak, Relative grain boundary energies from triple junction geometry: Limitations to assuming the Herring condition in nanocrystalline thin films, *Acta Mater.* **242**, 118476 (2023).

[11] U. Czubayko, V. G. Sursaeva, G. Gottstein, and L. S. Shvindlerman, Influence of triple junctions on grain boundary motion, *Acta Mater.* **46**, 5863 (1998).

[12] G. Gottstein, V. Sursaeva, and L. S. Shvindlerman, The effect of triple junctions on grain boundary motion and grain microstructure evolution, *Interface Sci.* **7**, 273 (1999).

[13] G. Gottstein, A. H. King, and L. S. Shvindlerman, The effect of triple-junction drag on grain growth, *Acta Mater.*

48, 397 (2000).

[14] G. Gottstein and L. S. Shvindlerman, Grain boundary junction engineering, *Scr. Mater.* **54**, 1065 (2006).

[15] A. H. King, The geometric and thermodynamic properties of grain boundary junctions, *Interface Sci.* **7**, 251 (1999).

[16] O. A. Shenderova and D. W. Brenner, Atomistic simulations of structures and mechanical properties of  $\langle 011 \rangle$  tilt grain boundaries and their triple junctions in diamond, *Phys. Rev. B* **60**, 7053 (1999).

[17] S. Shekhar and A. H. King, Strain fields and energies of grain boundary triple junctions, *Acta Mater.* **56**, 5728 (2008).

[18] S. L. Thomas, C. Wei, J. Han, Y. Xiang, and D. J. Srolovitz, Disconnection description of triple-junction motion, *Proc. Natl. Acad. Sci. U.S.A.* **116**, 8756 (2019).

[19] C. Wei, L. Zhang, J. Han, D. J. Srolovitz, and Y. Xiang, Grain boundary triple junction dynamics: A continuum disconnection model, *SIAM J. Appl. Math.* **80**, 1101 (2020).

[20] A. Caro and H. Van Swygenhoven, Grain boundary and triple junction enthalpies in nanocrystalline metals, *Phys. Rev. B* **63**, 134101 (2001).

[21] M. Li and T. Xu, Topological and atomic scale characterization of grain boundary networks in polycrystalline and nanocrystalline materials, *Prog. Mater Sci.* **56**, 864 (2011).

[22] G. Gottstein, L. S. Shvindlerman, and B. Zhao, Thermodynamics and kinetics of grain boundary triple junctions in metals: Recent developments, *Scr. Mater.* **62**, 914 (2010).

[23] S. M. Eich and G. Schmitz, Embedded-atom study of low-energy equilibrium triple junction structures and energies, *Acta Mater.* **109**, 364 (2016).

[24] N. Tuchinda and C. A. Schuh, Triple junction excess energy in polycrystalline metals, *Acta Mater.* **279**, 120274 (2024).

[25] J. P. Hirth and J. Lothe, *Theory of Dislocations*, 2nd ed. (Krieger Publishing Company, Malabar, Florida, USA, 1992).

[26] G. P. Dimitrakopoulos, T. H. Karakostas, and R. C. Pond, The defect character of interface junction lines, *Interface Sci.* **4**, 129 (1997).

[27] R. C. Pond and V. Vítek, Periodic grain boundary structures in aluminium I. A combined experimental and theoretical investigation of coincidence grain boundary structure in aluminium, *Proc. R. Soc. Lond. A* **357**, 453 (1997).

[28] J. C. Hamilton, D. J. Siegel, I. Daruka, and F. Léonard, Why do grain boundaries exhibit finite facet lengths?, *Phys. Rev. Lett.* **90**, 246102 (2003).

[29] D. L. Medlin, K. Hattar, J. A. Zimmerman, F. Abdeljawad, and S. M. Foiles, Defect character at grain boundary facet junctions: Analysis of an asymmetric  $\Sigma = 5$  grain boundary in Fe, *Acta Mater.* **124**, 383 (2017).

[30] R. Hadian, B. Grabowski, M. W. Finnis, and J. Neugebauer, Migration mechanisms of a faceted grain boundary, *Phys. Rev. Mater.* **2**, 043601 (2018).

[31] T. Brink, L. Langenohl, S. Pemma, C. H. Liebscher, and G. Dehm, Stable nanofacets in  $[111]$  tilt grain boundaries of face-centered cubic metals, *Phys. Rev. Mater.* **8**, 063606 (2024).

[32] Y. Choi and T. Brink, Faceting transition in aluminum as a grain boundary phase transition, *Phys. Rev. Mater.* **9**, 083607 (2025).

[33] T. Frolov, D. L. Medlin, and M. Asta, Dislocation content of grain boundary phase junctions and its relation to grain boundary excess properties, *Phys. Rev. B* **103**, 184108 (2021).

[34] L. Langenohl, T. Brink, R. Freitas, T. Frolov, G. Dehm, and C. H. Liebscher, Dual phase patterning during a congruent grain boundary phase transition in elemental copper, *Nat. Commun.* **13**, 3331 (2022).

[35] I. S. Winter and T. Frolov, Quantifying and visualizing the microscopic degrees of freedom of grain boundaries in the Wigner–Seitz cell of the displacement-shift-complete lattice, *Acta Mater.* **291**, 120968 (2025).

[36] E. W. Hart, Two-dimensional phase transformation in grain boundaries, *Scr. Metall.* **2**, 179 (1968).

[37] E. W. Hart, Grain boundary phase transformations, in *The Nature and Behavior of Grain Boundaries*, edited by H. Hu (Plenum Press, New York, USA, 1972) pp. 155–170.

[38] W. Cahn, J., Transitions and phase equilibria among grain boundary structures, *J. Phys. Colloques* **43**, C6 (1982).

[39] C. Rottman, Theory of phase transitions at internal interfaces, *J. Phys. Colloques* **49**, C5 (1988).

[40] T. Frolov and Y. Mishin, Thermodynamics of coherent interfaces under mechanical stresses. I. Theory, *Phys. Rev. B* **85**, 224106 (2012).

[41] T. Frolov and Y. Mishin, Thermodynamics of coherent interfaces under mechanical stresses. II. Application to atomistic simulation of grain boundaries, *Phys. Rev. B* **85**, 224107 (2012).

[42] S. Saood, T. Brink, C. H. Liebscher, and G. Dehm, Microstates and defects of incoherent  $\Sigma 3$   $[111]$  twin boundaries in aluminum, *Acta Mater.* **243**, 118499 (2023).

[43] V. V. Zhakhovskii, N. A. Inogamov, Y. V. Petrov, S. I. Ashitkov, and K. Nishihara, Molecular dynamics simulation of femtosecond ablation and spallation with different interatomic potentials, *Appl. Surf. Sci.* **255**, 9592 (2009).

[44] NIST Interatomic Potentials Repository, National Institute of Standards and Technology, <https://www.ctcms.nist.gov/potentials>, <https://doi.org/10.18434/m37>.

[45] E. Chen, T. W. Heo, B. C. Wood, M. Asta, and T. Frolov, Grand canonically optimized grain boundary phases in hexagonal close-packed titanium, *Nat. Commun.* **15**, 7049 (2024).

[46] J. Madsen and T. Susi, The abTEM code: transmission electron microscopy from first principles [version 2; peer review: 2 approved], Open Res. Europe **1**, 10.12688/openres-europe.13015.2 (2021).

[47] J. W. Cahn, Thermodynamics of solid and fluid surfaces, in *Interfacial Segregation*, edited by W. C. Johnson and J. M. Blakely (American Society of Metals, Metals Park, OH, USA, 1979) pp. 379–399.

[48] H. B. Callen, *Thermodynamics and an Introduction to Thermostatistics*, 2nd ed. (John Wiley & Sons, New York, USA, 1985).

[49] T. Frolov, D. L. Olmsted, M. Asta, and Y. Mishin, Structural phase transformations in metallic grain boundaries, *Nat. Commun.* **4**, 1899 (2013).

[50] R. Hadian, B. Grabowski, and J. Neugebauer, GB code: A grain boundary generation code, *J. Open Source Softw.* **3**, 900 (2018).

[51] V. Volterra, Sur l'équilibre des corps élastiques multiples

ment connexes, *Annales scientifiques de l'École Normale Supérieure* **24**, 401 (1907).

[52] R. de Wit, Partial disclinations, *J. Phys. C: Solid State Phys.* **5**, 529 (1972).

[53] A. E. Romanov, Mechanics and physics of disclinations in solids, *Eur. J. Mech. A/Solids* **22**, 727 (2003).

[54] T. Brink, L. Langenohl, H. Bishara, and G. Dehm, Universality of grain boundary phases in fcc metals: Case study on high-angle [111] symmetric tilt grain boundaries, *Phys. Rev. B* **107**, 054103 (2023).

[55] S. Saood, T. Brink, C. H. Liebscher, and G. Dehm, Influence of variation in grain boundary parameters on the evolution of atomic structure and properties of [111] tilt boundaries in aluminum, *Acta Mater.* **268**, 119732 (2024).

[56] W. T. Read and W. Shockley, Dislocation models of crystal grain boundaries, *Phys. Rev.* **78**, 275 (1950).

[57] F. R. N. Nabarro, Mathematical theory of stationary dislocations, *Adv. Phys.* **1**, 269 (1952).